Nanoscale

COMMUNICATION

View Article Online
View Journal | View Issue

Cite this: *Nanoscale*, 2014, **6**, 5691

Hollow nickel nanocorn arrays as three-dimensional and conductive support for metal oxides to boost supercapacitive performance†

Received 28th February 2014
Accepted 25th March 2014

DOI: 10.1039/c4nr01119h

www.rsc.org/nanoscale

Dongliang Chao,‡[a] Xinhui Xia,‡[ab] Changrong Zhu,[a] Jin Wang,[a] Jilei Liu,[a] Jianyi Lin,[ac] Zexiang Shen*[a] and Hong Jin Fan*[a]

A novel three-dimensional (3D) metal/metal oxide core/branch array electrode has been fabricated as a supercapacitor electrode. Hollow Ni nanocorn arrays are constructed on Ni foams and act as a highly conductive and stable support to Co_3O_4 nanoflakes. Enhanced pseudocapacitive performance compared to bare Co_3O_4 nanosheets is demonstrated with high rate capability and excellent cycling stability.

1. Introduction

Among various advanced power source devices, supercapacitors are receiving wide attention due to their distinctive properties compared to conventional batteries, that is, fast charge–discharge rates, long lifespan, low maintenance cost and safety operation. Generally speaking, a high-performance supercapacitor electrode requires electrochemically stable materials, large surface areas, decent electrical conductivity and ion transport kinetics.[1]

Nanostructured transition metal oxides (such as MnO_2, Co_3O_4 and NiO) and their hybrids have high specific capacities and high energy densities due to their rich nanostructures with large surface areas and capability of interfacial redox electrochemical reactions.[2–6] However, most of these materials are intrinsically less conductive, which makes them kinetically deficient to support the fast electron transport required by high power applications. In this context, utilization of nano-featured conductive frameworks as the substrates (or current collectors) for the electrochemically active materials is one of the effective strategies to boost the energy density and power density.[7–10] Metallic substrates, such as Ti foil, Ni foil, stainless steel, and Ni foam, have been commonly employed to improve the pseudocapacitive performance of oxide electrodes.[11–14] However, their flat surfaces or micron-grade pores severely limit the loading of active materials; a metallic substrate with a higher porosity with submicron or nano-sized features is more favorable. A three-dimensional (3D) conductive metal framework, which is ideally suited for electrodes in batteries, supercapacitors, electrochemical catalysis and fuel cells, has been a very intriguing topic for decades.[15–17] To date only a very limited number of 3D nano-sized metal framework structures have been realized in some very particular material systems. For example, porous metal Ni and Au networks were obtained by a de-alloying process,[18,19] and microporous dendritic nano-Ni and nano-Cu films were formed by electrodeposition.[15,20] However, there are relatively few demonstrations of enhanced pseudocapacitive performance based on the above porous nano-metal substrates.

In this work, we constructed a new type of hollow corn-like Ni nanoarray as the support for subsequent growth of mesoporous Co_3O_4 thin nanosheets. In this design, the Ni nanocorns are in rigid contact with the Ni foam; they increase the surface area of the Ni foam (current collector) and hence the loading of active materials. This effectively increases the porosity of the whole electrode, which can lead to high capacity and high energy density. As a proof-of-concept demonstration of its electrochemical energy storage application, we have characterized the Ni/Co_3O_4 CBAs as working electrodes for supercapacitors. Our results show that these Ni/Co_3O_4 CBAs electrodes can exhibit a high capacitance (705 F g^{-1} at 40 A g^{-1}), which is much larger than that of Co_3O_4 nanosheets grown directly on nickel foam (247 F g^{-1} at 40 A g^{-1}), a good rate capability (91% capacitance retention at 40 A g^{-1}), and an excellent cycling stability (only 5% loss after 10 000 cycles). Moreover, this new electrode also exhibits shortened activation cycles for Co_3O_4, which increases the initial utilization of the electrode.

[a]*Division of Physics and Applied Physics, School of Physical and Mathematical Sciences, Nanyang Technological University, 637371, Singapore. E-mail: fanhj@ntu.edu.sg*

[b]*State Key Laboratory of Silicon Materials, Key Laboratory of Advanced Materials and Applications for Batteries of Zhejiang Province, and Department of Materials Science and Engineering, Zhejiang University, Hangzhou 310027, China*

[c]*Heterogeneous Catalysis, Institute of Chemical Engineering and Sciences, A*star, 1 Pesek Road, Jurong Island, 627833, Singapore*

† Electronic supplementary information (ESI) available. See DOI: 10.1039/c4nr01119h

‡ These authors contributed equally to this work.

2. Experimental

2.1 Preparation of hollow Ni nanorod arrays

First, atomic layer deposition (ALD, Beneq, TFS 200) of ZnO as the seed layer was conducted at 200 °C on various substrates (Ni foam, Ti foil, stainless steel foil) using diethylzinc ($Zn(C_2H_5)_2$, DEZ) and water as the zinc and oxygen source, respectively. The ALD ZnO-coated substrates were immersed into a 100 mL aqueous solution containing 0.1 M zinc nitrate ($Zn(NO_3)_2 \cdot 6H_2O$) and 0.1 M hexamethylenetetramine ($C_6H_{12}N_4$) in an autoclave. The reaction was conducted at 95 °C for 5 h. Finally, the Ni electrodeposition was performed in a standard three-electrode glass cell at 25 °C, using the above ZnO nanoarray as the working electrode, Ag/AgCl as the reference electrode, and a Pt foil as the counter electrode. The Ni was electrodeposited from an aqueous solution containing 0.02 M Ni_2SO_4 and 0.04 M NH_4Cl at a constant current of 0.5 mA cm^{-2} for 1800 s. After electrodeposition, the samples were washed with a 5 mM hydrochloric acid in water solution for 10 min to remove the ZnO nanorod template, resulting in a hollow Ni nanorod array.

2.2 Preparation and characterization of Ni/Co_3O_4 core/branch arrays

Following the formation of hollow Ni nanocorn arrays, $Co(OH)_2$ nanoflakes were grown through a facial cathodic electrodeposition method in a standard three-electrode glass cell at 25 °C. The electrolyte for electrodeposition was obtained by dissolving 6 g $Co(NO_3)_2 \cdot 6H_2O$ in 100 mL of distilled water. The electrodeposition of $Co(OH)_2$ was done at a constant current of 0.6 mA cm^{-2} for 2400 s. The electrodeposition processes included an electrochemical reaction and a precipitation reaction, expressed as follows:

$$NO_3 + H_2O + 2e^- \rightarrow NO_2^- + 2OH^- \quad (1)$$

$$Co^{2+} + 2OH^- \rightarrow Co(OH)_2 \quad (2)$$

After deposition, the sample was then annealed at 200 °C in air for 1.5 h in order to convert $Co(OH)_2$ to mesoporous Co_3O_4 branches. For comparison, the Co_3O_4 nanosheets were also electrodeposited under the same conditions on a bare nickel foam substrate.

2.3 Characterization and electrochemical measurements

The morphologies of the samples were characterized using field emission scanning electron microscopy (FESEM, FEI SIRION). The detailed nanostructures of the samples were investigated using high-resolution transmission electron microscopy (HRTEM, JEOL JEM-2010F) operating at 200 kV. The crystal structures of the samples were identified using X-ray diffraction (XRD, RigakuD/Max-2550 with Cu Kα radiation). A Raman spectrum was obtained with a WITec-CRM200 Raman system (WITec, Germany) and a laser wavelength of 532 nm (2.33 eV). The Si peak at 520 cm^{-1} was used as a reference to calibrate the wavenumber.

Electrochemical measurements were performed in a tri-electrode cell consisting of a working electrode (core/branch arrays), a platinum plate counter electrode and an Hg/HgO reference electrode in a 2 M KOH electrolyte solution. Electrochemical performance was evaluated by galvanostatic charge–discharge tests (LAND battery testing system), cyclic voltammetry (CV), and electrochemical impedance spectroscopy (EIS) measurements (CHI660C electrochemical workstation). CV measurements were carried out at different scanning rates between 0.1 and 0.6 V at 25 °C. For EIS, the amplitude of the sine perturbation signal was 5 mV, and the frequency was scanned from the highest (100 kHz) to the lowest (10 mHz) value. The area of the electrode is ~4 cm^2. The mass of Ni nanocorn arrays was ~1.0 mg cm^{-2}, and that of Co_3O_4 nanoflakes was ~0.8 mg cm^{-2}. The specific capacitance C_g (unit of F g^{-1}) was calculated as:

$$C_g = \frac{I\Delta t}{M\Delta V} \quad (3)$$

where I (mA), Δt (s), ΔV (V) and M (mg) represent the discharge current, total discharge time, potential drop during discharge and mass of electrode materials, respectively.

3. Results and discussion

The general fabrication procedure of the hollow metal/metal oxide core/branch arrays (CBA) is illustrated in Fig. 1. First, ZnO nanorod templates were grown on conductive substrates following the standard hydrothermal synthesis method. Second, a thin layer of metal particles was electrodeposited along the surface of ZnO nanorods (see Fig. 1(b)). After that, the as-obtained ZnO/Ni nanorod arrays were bathed in 5 mM hydrochloric acid for 10 min in order to remove the ZnO core

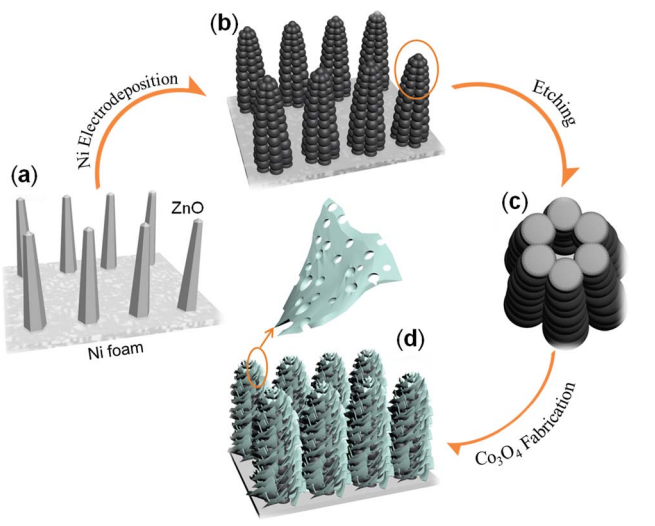

Fig. 1 Schematics of the fabrication process of metal/oxide CBA. (a) ZnO nanorod template by hydrothermal synthesis (ALD ZnO as seed layer). (b) ZnO/Ni nanorods after electrochemical deposition of Ni. (c) Top view of a single hollow nickel nanocorn after etching the ZnO nanorods. (d) Ni/Co_3O_4 CBAs by electrodeposition growth of mesoporous Co_3O_4 nanoflakes.

and achieve hollow Ni nanocorn arrays. Finally, a uniform coverage of the Ni nanocorns by mesoporous Co_3O_4 nanoflake branches was realized by another round of electrodeposition combined with a short post annealing treatment. With this method, we have successfully prepared Ni/Co_3O_4 CBAs on nickel foam, Ti foil and stainless steel foil. Such unique electrode architectures promise fast electron transport by direct connection to the conductive Ni nanocorn and facile ion diffusion provided by the hollow structure in both the nanocorns and the Co_3O_4 nanoflakes.

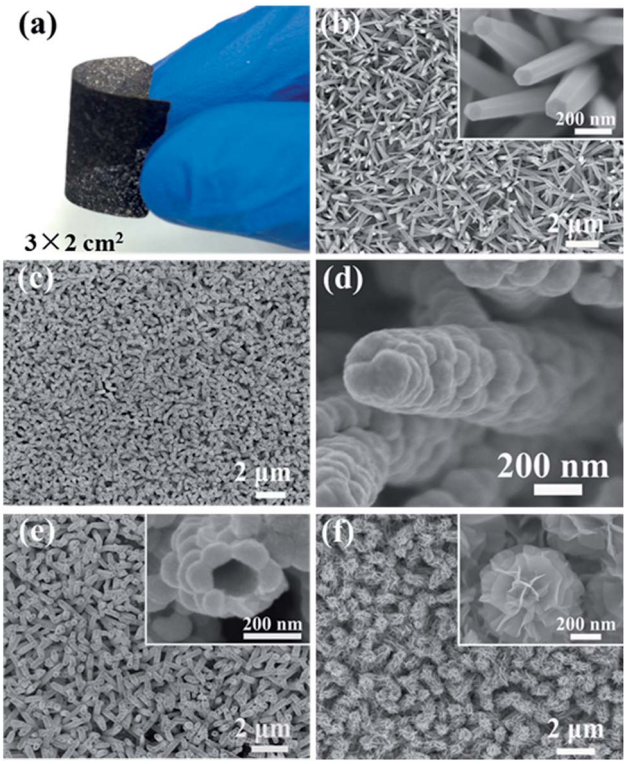

Fig. 2 (a) Photograph of a severely bent Ni/Co_3O_4 CBA sample with a size of 3 × 2 cm^2; (b) SEM image of ZnO nanorod template; (c) and (d) SEM images of ZnO/Ni nanoarrays; (e) SEM image of hollow nickel nanocorn arrays; (f) SEM image of Ni/Co_3O_4 CBAs. Insets are the corresponding magnified views.

Fig. 2(a) shows a photograph of a 3 × 2 cm^2 Ni/Co_3O_4 CBA grown on a Ni foam sample. The as-grown CBA materials have good adhesion to the Ni foam, as it can be severely bent (>150°) without detachment of the as-grown materials. The SEM image in Fig. 2(b) presents a uniform and near-vertically aligned ZnO nanorod substrate with a diameter about 100 nm and an approximate height of about 1–2 μm. Each ZnO nanorod has evident hexagonal facets (inset of Fig. 2(b)), which is characteristic of its hcp crystal structure.[21,22] The diffraction peaks at 31.9°, 34.5° and 36.4° can be well indexed to wurtzite structure of (100), (002) and (101) planes of ZnO (JCPDS 36-1451).[22]

After the electrodeposition of Ni (30 min), the nanorod array structure is well preserved, but each nanorod becomes thicker and rougher because of a full coverage of Ni particles (see Fig. 2(c) and (d)). During this process, the semiconducting ZnO nanorods act as the backbone to guide the nucleation deposition of Ni. The growth mechanism of the Ni nanoparticle shell can be well understood based on previous reports.[23,24] To see it clearly, we also conducted time-control experiments (see Fig. 3(a)–(c)). Heterogeneous nucleation on ZnO nanorods occurs when Ni nanocrystallites precipitate in the supersaturated solution, which is a process of surface energy minimization. The early-stage nucleation of Ni along the surface of ZnO nanorods can be seen by a sparse attachment of some small particles after 5 min deposition. With increasing deposition time, these nanoparticles grow and merge, until they eventually form a continuous layer of Ni particles covering the entire ZnO nanorod surface (see Fig. 3 (c)).

After the removal of ZnO nanorod templates, the obtained hollow Ni nanocorn arrays are still firmly adhered to the substrates. The hollow interior can be seen clearly from a top view in Fig. 2(e). The typical interval between Ni nanocorns is about 500 nm, which is large enough for subsequent growth of

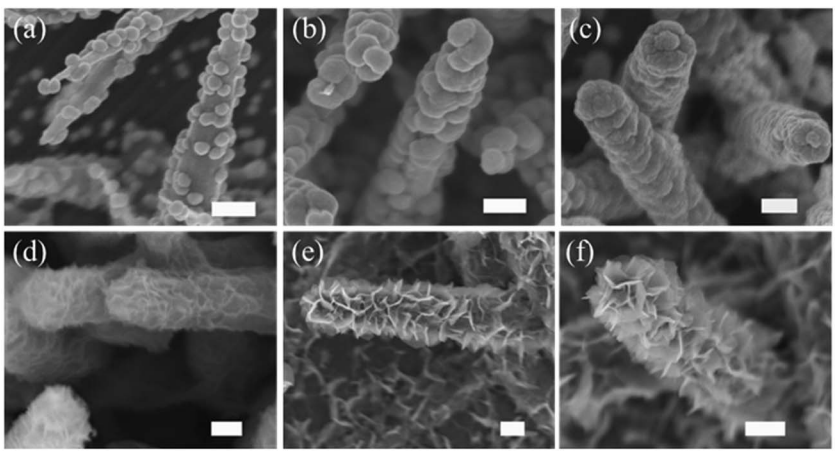

Fig. 3 Time-control experiments to reveal the morphological evolution. (a–c) SEM images of the ZnO/Ni nanostructure obtained after electrochemical deposition of Ni for different times: (a) 5 min; (b) 15 min; (c) 30 min; (d–f) SEM images of the Ni/Co_3O_4 CBA after electrochemical deposition of Co_3O_4 for different times: (d) 10 min; (e) 20 min; (f) 40 min. Scale bars: 200 nm.

metal oxide branches. After the electrochemical deposition and thermal annealing, the Ni nanocorns are decorated homogeneously with numerous Co_3O_4 thin nanoflakes (thickness around 10 nm), as seen clearly in Fig. 2(f). The "oriented" growth mechanism of the nanoflakes during electrodeposition has been elaborated previously.[5,25,26] Briefly, in the early stage OH^- ions are absorbed onto the surface of the Ni nanocorns; the OH^- ions then react with the neighbor Co^{2+} to form the initial $Co(OH)_2$ crystals. These crystals will serve as nuclei for the subsequent growth of $Co(OH)_2$ nanoflakes *via* self assembly. These processes are also disclosed by results of the time-control experiments (see Fig. 3 (d)–(f)). It is noteworthy that similar Ni/Co_3O_4 CBAs can also be readily fabricated on other conductive substrates (such as Ti and stainless steel foil, see ESI Fig. S1†). Given the versatility of the electrodeposition technique for other metal oxides,[23–25] our fabrication method for metal/metal oxide CBAs is general.

Further insight into the detailed microstructure of the Ni/Co_3O_4 CBAs was obtained by TEM investigations. Fig. 4(a) shows clearly the hollow interior of the nickel nanocorn after etching of a ZnO nanorod with a diameter of about 100 nm. This can also be confirmed by the X-ray diffraction (XRD) pattern of hollow Ni nanocorn in Fig. S2(a)† where the peaks of ZnO disappear. The HRTEM and selected area electron diffraction (SAED) pattern recorded from the nanocorn reveal a polycrystalline nature, and the lattice spacing of 0.20 nm agrees with the (111) plane of the Ni phase (Fig. 4(b)). The Ni/Co_3O_4 CBA structure can also be easily distinguished from the TEM image (Fig. 4(c)). The Ni core nanorod is tightly wrapped with the Co_3O_4 branched nanoflakes; the flakes possess nanocrystallites of about 10 nm in size and numerous nanopores ranging from 3 to 5 nm (Fig. 4(d)). This hollow core and unique mesoporous branching is good for electrolyte penetration and ion/electron transfer, which may result in enhanced electrochemical properties. Besides, the corresponding polycrystalline FFT pattern (inset in Fig. 4(d)) of the branched nanoflakes can be well indexed to the spinel Co_3O_4, and the lattice fringes with lattice spacing of 0.46 and 0.24 nm are in good agreement with the (111) and (311) planes of Co_3O_4, respectively. XRD pattern shows that, in addition to the three strong peaks associated with the Ni foam substrate and Ni nanocorn array, the peaks located at 19.0°, 36.8° and 65.2° can be identified to be (111), (311) and (440) diffraction signals of spinel Co_3O_4 phase (JCPDS 42-1467) (Fig. S2(a)†). The phase is also supported by Raman peaks at around 476, 516, 615, and 683 cm^{-1}, corresponding to the E_g, F^1_{2m},F^2_{2g} and A_{1g} modes of Co_3O_4 (see Fig. S2(b)†).

The Ni/Co_3O_4 CBAs are applied as additive-free pseudocapacitive electrodes and demonstrate evidently improved properties compared to pure Co_3O_4 nanosheets without hollow Ni nanocorn support. Herein, Ni/Co_3O_4 CBAs grown on nickel foam were chosen for characterization, and the electrochemical properties are presented in Fig. 5. In order to highlight the electrochemical superiority of the Ni/Co_3O_4 CBAs, Co_3O_4 nanosheets grown directly on Ni foam (see SEM and TEM images in Fig. S3†) are also studied for comparison. Fig. 5(a) shows the cyclic voltammograms (CV) of both types of electrodes at a scan rate of 10 mV s^{-1}. A pair of symmetric anodic and cathodic peaks can be easily observed on each branch of the CV curve in a potential range of 0.1 to 0.6 V, implying the existence of two pseudocapacitive behaviors or reversible faradaic reactions of the tested samples. For the Co_3O_4 nanosheet electrode, it is well accepted that the first redox reaction is related to the reaction of $Co_3O_4 \leftrightarrow CoOOH$, and the second redox reaction corresponds to the conversion between CoOOH and CoO_2 (approximate peak position is added in Fig. 5(a)). The Ni/Co_3O_4 CBA electrode shows similar CV behavior but with different encircling areas and peak positions. The encircling area of the Ni/Co_3O_4 CBA electrode is much larger than that of the Co_3O_4 nanosheet electrode, indicating a much higher electrochemical activity and capacitance for Ni/Co_3O_4 CBAs than for Co_3O_4 nanosheets. It can be seen easily from the CV curves that the two oxidation (reduction) peaks of the Ni/Co_3O_4 CBA electrode are located at 0.442 and 0.513 V (0.389 and 0.504 V). As a comparison, the two oxidation (reduction) peaks of the Co_3O_4 nanosheet electrode shift to 0.458 and 0.532 V (0.372 and 0.502 V). Generally, the smaller potential separation of the Ni/Co_3O_4 CBA electrode indicates a better reversibility/weaker polarization. It can be seen that CVs of Ni/Co_3O_4 retain a similar shape even at high sweep rates (see Fig. S4(a)†); this is an indication of an excellent capacitance behavior and the fast diffusion of electrolyte ions into the Ni/Co_3O_4 CBAs.

Fig. 5(b) compares the charge–discharge curves of both Co_3O_4 nanosheets and Ni/Co_3O_4 CBAs in a potential range of 0–0.55 V (*vs.* Hg/HgO) at a galvanostatic charge–discharge current density of 2 A g^{-1}. It can be seen that the Ni/Co_3O_4 CBA electrode provides a lower charge plateau and a higher discharge plateau. Again, this is a manifestation of a smaller polarization and lower internal resistance than that of the Co_3O_4 nanoflake electrode. This can be confirmed by the Nyquist plots in

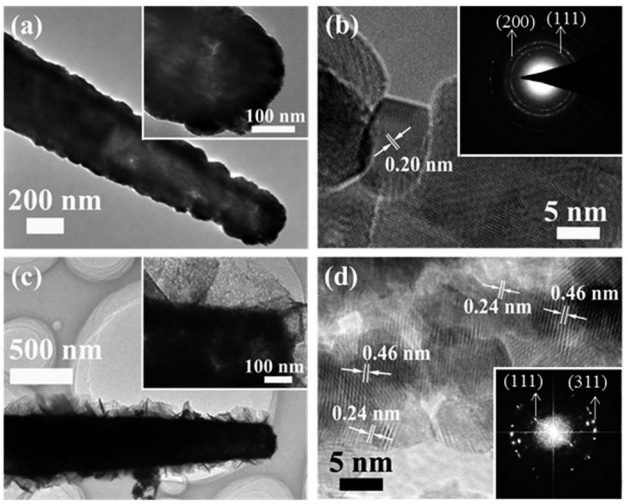

Fig. 4 TEM images of the nanostructure at different fabrication stages. (a) Hollow nickel nanocorn after etching the ZnO nanorod core (inset is the enlarged view of the hollow interior); (b) HRTEM image of Ni nanocorn wall (inset is the SAED pattern); (c) after growth of Co_3O_4 nanoflake branches (inset is a magnified TEM image of a Co_3O_4 nanoflake); (d) HRTEM image of the Co_3O_4 nanoflake (inset is the corresponding FFT pattern).

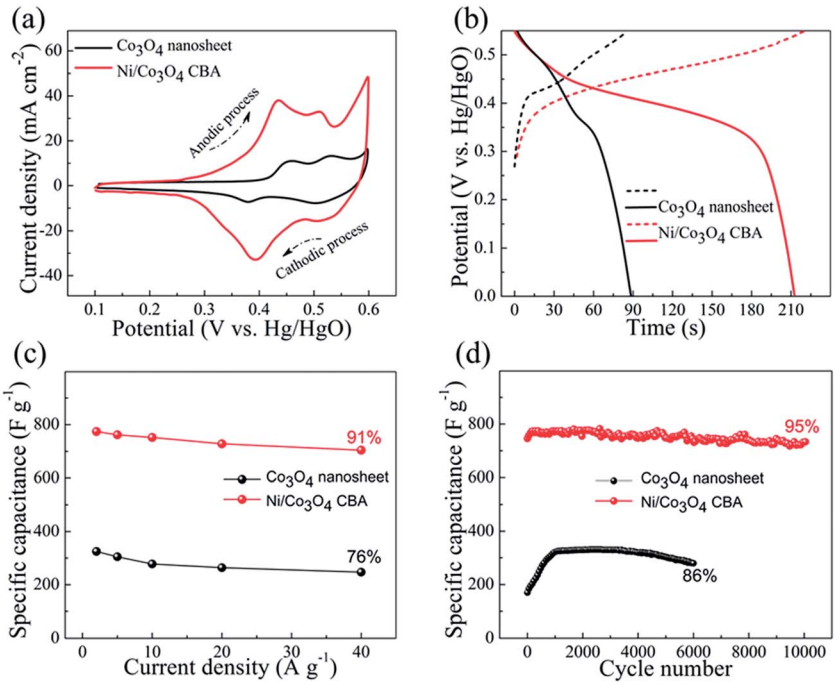

Fig. 5 Electrochemical pseudocapacitive property of Co_3O_4 nanosheets and Ni/Co_3O_4 CBAs grown on nickel foam: (a) CV curves at a scanning rate of 10 mV s^{-1}; (b) charge–discharge curves at 2 A g^{-1} after the electrode was activated by cycling 1000 times; (c) specific capacitances at different current densities; and (d) cycling performances at 2 A g^{-1}.

Fig. S4(b).† A large semicircle relates to a large charge transfer resistance, and a steep slope means a low diffusion rate. Obviously, the Ni/Co_3O_4 CBA electrode exhibits a much smaller semicircle and slower slope, corresponding to a smaller charge transfer resistance on the surface of the material and a higher diffusion rate in the bulk of the electrode than that of the Co_3O_4 nanosheet electrode. The galvanostatic discharge curves of both the Ni/Co_3O_4 CBA electrode and pure Co_3O_4 nanosheet electrode at various current densities are shown in Fig. S4(c) and (d).† Based on the discharge curves, the specific capacitances were calculated and plotted in Fig. 5(c). The specific capacitance is calculated based on the mass of Co_3O_4 nanosheets for the Co_3O_4 nanosheet electrode, and the total mass of Ni nanocorn plus Co_3O_4 nanoflakes for the Ni/Co_3O_4 CBA electrode. The specific capacitance for the Ni/Co_3O_4 CBA electrode ranges from 780 F g^{-1} at 2 A g^{-1} to 705 F g^{-1} at 40 A g^{-1}. Comparatively, the Co_3O_4 nanosheet electrode shows a specific capacitance ranging from 325 F g^{-1} at 2 A g^{-1} to 247 F g^{-1} at 40 A g^{-1}. Therefore, when the current increases from 2 A g^{-1} to 40 A g^{-1}, the Ni/Co_3O_4 CBA electrode can retain 91% of the initial capacitance while this percentage is only 76% for the Co_3O_4 nanosheet electrode. These capacitance values are also much higher than those for our previous self-supported hollow Co_3O_4 nanowire arrays (599 F g^{-1} at 2 A g^{-1}, 73% rate capacitance retention),[27] porous Co_3O_4 film (443 F g^{-1} at 2 A g^{-1}, 76% rate capacitance retention),[28] and some other reports,[29,30] and comparable to that of brush-like nanowires (784 at 40 A g^{-1}, 86% rate capacitance retention).[31] This good rate retention is very important for high-power supercapacitor applications. When the total mass of the electrode (including the Ni foam, 30 mg cm^{-2}) is included in the calculation, the capacitance of the Ni/Co_3O_4 CBA electrode is ~45 F g^{-1}, which is still much higher than that of the Co_3O_4 nanosheet electrode (~8 F g^{-1}).

To highlight the superior electrochemical performance of the as prepared Ni/Co_3O_4 CBA electrode, cycling response up to 10 000 cycles was recorded at a current density of 2 A g^{-1}. As shown in Fig. 5(d), the capacitance exhibits negligible loss (~5%) even after a continuous 10 000 cycles, much better than that of the Co_3O_4 nanosheet electrode, which shows a worse cycling stability with a 14% capacitance loss after 6000 cycles at a current density of 2 A g^{-1}. Generally, before the device can deliver the highest capacitance, an "activation process" can be observed and is indicated by a gradual capacitance increase within the first 400–1000 cycles; this is related to the electrolyte penetration into the core of the Co_3O_4 electrode.[2,27,28,31,32] A long activation process will certainly result in a low utilization of active materials, and thus low energy, during the first several hundred cycles. In our case, the Ni/Co_3O_4 CBA delivers a high initial discharge capacitance of ~735 F g^{-1} and takes less than 100 cycles to reach its highest capacitance (780 F g^{-1}). The difference between the highest capacitance and initial discharge capacitance is small enough to give a high initial utilization and energy. In sharp contrast, the Co_3O_4 nanosheets directly grown on nickel foam take nearly 1000 cycles to be fully activated. In addition, it is well know from our previous results that the nickel foam substrate also shows a redox process due to the reversible reaction of NiOOH/$Ni(OH)_2$ formed after the activation process (Ni/NiOOH) on the nickel surface.[2,32] Our previous work also proved that the capacitance contribution from the nickel foam is quite small (<5%) and increases up to a

stable value after about 500 cycles. Thus, in order to minimize the effect from substrate in our case, all specific capacitances are calculated after subtracting the discharge time of the nickel foam.[2] The CBA architecture of the Ni/Co_3O_4 electrode is well preserved after 10 000 cycles (see SEM image in Fig. S5†), thanks to the rigid contact of the mesoporous Co_3O_4 flakes to the Ni nanocorns.

The enhanced pseudocapacitive performance of the Ni/Co_3O_4 CBA electrode can be ascribed to the beneficial features of the hollow Ni nanocorn support. The hollow Ni nanocorns reduce the internal resistance, shorten the ion diffusion paths and therefore facilitate the carrier transport kinetics. They also effectively increase the loading of active materials of Co_3O_4 nanosheets more than bare nickel foams and provide more active sites for Faraday reactions. The above properties will result in an effectively higher capacitance, superior rate performance and shorter activation process. In addition, the redox process of the Ni nanocorn may also have contributed to the total capacitance. For the superior cycling stability, the Ni/Co_3O_4 CBA structure may help to stabilize the array morphology and alleviate the volume expansion of Co_3O_4 upon long cycles.

4. Conclusion

We have demonstrated a porous Ni/Co_3O_4 core/branch array (CBA) as an interesting pseudocapacitive material, which exhibits evidently superior electrochemical properties compared to pure Co_3O_4 nanosheets without the Ni support. The CBA is composed of a new kind of corn-like hollow Ni nanorods as the core and mesoporous Co_3O_4 nanosheets as the branches. Such Ni/Co_3O_4 CBAs exhibit a high specific capacitance (~705 F g^{-1} at 40 A g^{-1}), an excellent rate capability (~91% retention relative to 2 A g^{-1}), and an outstanding cycling performance (~95% capacitance retained after 10 000 cycles). The performance enhancement could be exclusively attributed to the unique hollow Ni nanocorn arrays, which are highly conductive and allow more efficient loading of active materials and sufficient access of electrons/ions, as well as enhanced structural integrity. Given the versatility of the electrodeposition technique for both metal and metal oxides, our design protocol can be applied to many other hybrid systems for the high-potential electrochemical applications in Li ion batteries, supercapacitors, and catalysis.

Acknowledgements

This work is supported by SERC Public Sector Research Funding (Grant number 1121202012), Agency for Science, Technology, and Research (A*STAR), Singapore. The authors also acknowledge support from the Energy Research Institute @NTU (ERI@N).

References

1 H. G. Zhang, X. D. Yu and P. V. Braun, *Nat. Nanotechnol.*, 2011, **6**, 277–281.
2 X. H. Xia, J. P. Tu, Y. Q. Zhang, X. L. Wang, C. D. Gu, X. B. Zhao and H. J. Fan, *ACS Nano*, 2012, **6**, 5531–5538.
3 T. Y. Wei, C. H. Chen, H. C. Chien, S. Y. Lu and C. C. Hu, *Adv. Mater.*, 2010, **22**, 347–351.
4 J. X. Zhu, Z. Y. Yin, H. Li, H. T. Tan, C. L. Chow, H. Zhang, H. H. Hng, J. Ma and Q. Y. Yan, *Small*, 2011, **7**, 3458–3464.
5 J. P. Liu, J. Jiang, C. W. Cheng, H. X. Li, J. X. Zhang, H. Gong and H. J. Fan, *Adv. Mater.*, 2011, **23**, 2076–2081.
6 Q. Li, Z. L. Wang, G. R. Li, R. Guo, L. X. Ding and Y. X. Tong, *Nano Lett.*, 2012, **12**, 3803–3807.
7 C. Cheng and H. J. Fan, *Nano Today*, 2012, **7**, 327–343.
8 G. Yu, X. Xie, L. Pan, Z. Bao and Y. Cui, *Nano Energy*, 2013, **2**, 213–234.
9 W. Wang, S. R. Guo, K. N. Bozhilov, D. Yan, M. Ozkan and C. S. Ozkan, *Small*, 2013, **9**, 3714–3721.
10 X. Dong, J. Wang, J. Wang, M. B. Chan-Park, X. Li, L. Wang, W. Huang and P. Chen, *Mater. Chem. Phys.*, 2012, **134**, 576–580.
11 J. Jiang, J. P. Liu, W. W. Zhou, J. H. Zhu, X. T. Huang, X. Y. Qi, H. Zhang and T. Yu, *Energy Environ. Sci.*, 2011, **4**, 5000–5007.
12 H. W. Wang, Y. L. Wang and X. F. Wang, *Electrochem. Commun.*, 2012, **18**, 92–95.
13 X. Xia, C. Zhu, J. Luo, Z. Zeng, C. Guan, C. F. Ng, H. Zhang and H. J. Fan, *Small*, 2014, **10**, 766–773.
14 T. Wang, Z. Peng, Y. Wang, J. Tang and G. Zheng, *Sci. Rep.*, 2013, **3**, 2693.
15 H. C. Shin, J. Dong and M. L. Liu, *Adv. Mater.*, 2003, **15**, 1610–1614.
16 W. Wang, M. Tian, A. Abdulagatov, S. M. George, Y. C. Lee and R. G. Yang, *Nano Lett.*, 2012, **12**, 655–660.
17 K. Flomin, I. Jen-La Plante, B. Moshofsky, M. Diab and T. Mokari, *Nanoscale*, 2014, **6**, 1335–1339.
18 J. K. Chang, C. M. Wu and I. W. Sun, *J. Mater. Chem.*, 2010, **20**, 3729–3735.
19 X. Y. Lang, A. Hirata, T. Fujita and M. W. Chen, *Nat. Nanotechnol.*, 2011, **6**, 232–236.
20 X. H. Xia, J. P. Tu, Y. Q. Zhang, Y. J. Mai, X. L. Wang, C. D. Gu and X. B. Zhao, *J. Phys. Chem. C*, 2011, **115**, 22662–22668.
21 M. Riaz, J. Song, O. Nur, Z. L. Wang and M. Willander, *Adv. Funct. Mater.*, 2011, **21**, 628–633.
22 X. C. Dong, Y. F. Cao, J. Wang, M. B. Chan-Park, L. H. Wang, W. Huang and P. Chen, *RSC Adv.*, 2012, **2**, 4364–4369.
23 G. R. Li, H. Xu, X. F. Lu, J. X. Feng, Y. X. Tong and C. Y. Su, *Nanoscale*, 2013, **5**, 4056–4069.
24 Y. B. He, G. R. Li, Z. L. Wang, C. Y. Su and Y. X. Tong, *Energy Environ. Sci.*, 2011, **4**, 1288–1292.
25 X. H. Xia, J. P. Tu, Y. Q. Zhang, J. Chen, X. L. Wang, C. D. Gu, C. Guan, J. S. Luo and H. J. Fan, *Chem. Mater.*, 2012, **24**, 3793–3799.
26 L. Q. Mai, F. Yang, Y. L. Zhao, X. Xu, L. Xu and Y. Z. Luo, *Nat. Commun.*, 2011, **2**, 381–385.
27 X. H. Xia, J. P. Tu, Y. J. Mai, X. L. Wang, C. D. Gu and X. B. Zhao, *J. Mater. Chem.*, 2011, **21**, 9319–9325.
28 Y. F. Yuan, X. H. Xia, J. B. Wu, X. H. Huang, Y. B. Pei, J. L. Yang and S. Y. Guo, *Electrochem. Commun.*, 2011, **13**, 1123–1126.

29 S. K. Meher and G. R. Rao, *J. Phys. Chem. C*, 2011, **115**, 15646–15654.
30 J. H. Kwak, Y. W. Lee and J. H. Bang, *Mater. Lett.*, 2013, **110**, 237–240.
31 R. Rakhi, W. Chen, D. Cha and H. Alshareef, *Nano Lett.*, 2012, **12**, 2559–2567.
32 X. H. Xia, J. P. Tu, Y. Q. Zhang, Y. J. Mai, X. L. Wang, C. D. Gu and X. B. Zhao, *RSC Adv.*, 2012, **2**, 1835–1841.